# Physically based modelling on microstructural evolution of static recrystallisation in pure aluminium

Qinmeng Luan, Junyi Lee, Jing-Hua Zheng*, Christopher Hopper, Jun Jiang

Department of Mechanical Engineering, Imperial College London, London SW7 2AZ, UK

*Corresponding author. Email address: Jinghua.zheng13@imperial.ac.uk

## Abstract

An in-depth understanding of the recrystallization process in alloys is critical to manufacturing metal parts with superior properties. However, the development of recrystallization model under various processing conditions is still in its early research stage and becoming an urgent demand for both the manufacturing industry and scientific research. In this work, a validated numerical model that is capable of predicting the recrystallized grain structure, incubation time for the grain nucleation and texture evolution, was developed using a Kobayashi, Warren and Carter (KWC) phase-field model coupled with crystal plasticity finite element (CPFE) analysis. Through characterising the microstructure evolution of static recrystallization (SRX) by quasi-in-situ Electron Backscatter Diffraction (EBSD) mapping, insights into nucleation position, grain growth rate and orientation correlation between nucleated grains and initial grains were established and transferred into the computational model. This model enables a reliable and accurate prediction of recrystallized microstructure and texture for pure aluminium under different processing routes. It is believed that this physically-based modelling work in mesoscale will motivate further micromechanical modelling studies using crystal plasticity to predict the performance of structural alloys after thermomechanical processing.

*Keywords:* static recrystallization; quasi-in-situ EBSD; crystal plasticity finite element; phase-field model; rolled pure aluminium; incubation time

## 1. Introduction

The required engineering properties for aeroplane components, such as high strength, toughness and good fatigue and creep resistance, are attributed to a designed microstructure with homogeneous small grains, minimum impurity segregation and a high amount of finely dispersed precipitates [1]. Thermomechanical processing routes (TMP), during which recrystallization may take place, are required for alloys to achieve the desired microstructures in final products [2,3]. Therefore, in order to optimize the microstructure and obtain specific material properties for structural alloys, it is vital to understand, control and predict the recrystallization based on experiments, physical concepts and computational models [1,3]. A computational model that is capable of predicting microstructure evolution, crystallographic texture and mechanical properties in the course of recrystallization would substantially advance our understanding of microstructure control in structural components [4–6].

In the manufacturing industry, the capability to accurately predict basic microstructural parameters such as the evolution of recrystallization fraction and grain size under the real-world processing conditions is in high demand [6]. However, current models have limited accuracy when the processing routes contain temperature gradients and complex strain paths. This is because the deformed microstructure is not well established in these models [6]. Constructing a computational model to predict recrystallization on the basis of the inhomogeneities in the deformed structure, therefore, becomes a vital topic in both science and engineering [7,8].

The prediction on the deformed microstructure and occurrence of recrystallization has been achieved in our previous paper [9]. However, there are still three main problems regarding grain nucleation not addressed well in that paper due to the lack of experimental observations.

The first unsolved problem is the prediction of texture formation during recrystallization [2,9–12]. Experimental observations in this work on the orientations of nucleated grains in deformed structures would provide the experimental and theoretical support for the computational model to assign orientations for nucleated grains.

The prediction on nucleation sites based on the deformed structure is also challenging due to various affecting factors, such as the effect of dislocation density distribution, grain boundaries, shear bands, precipitates and their interactions [2,13]. The powerful in-situ electron backscattered diffraction (EBSD) technique [14] in this work enables us to visualize the position of nucleations and quantitatively analyse crystallographic features, such as (sub)grain

boundaries, grain boundary misorientations, geometrically necessary dislocations (GNDs), crystal orientations and local phases, such that, grain nucleation criteria and simulated recrystallization process can be calibrated against the experimental results.

The other unsolved feature of recrystallization is the incubation time of new grains during static recrystallization (SRX), coined as incubation time [2,3,15]. This is defined as the time necessary for nucleated sites to form large enough subgrains with sufficient driving force (i.e. sufficient energy difference compared with the surrounding deformed grains) to overcome the opposing pressure from the grain boundary curvature [2,3]. A physically-based phase-field model addressed in this work would help to determine the incubation time for recrystallized grains in a specific deformed state to reach the critical size, thus, providing a guideline for the processing routes consequently.

This work, for the first time, systematically examined and simulated the SRX behaviour of rolled pure aluminium using quasi-in-situ EBSD technique, CPFE and KWC phase-field model. The evolutions of grain sizes, textures and dislocations during soaking at 500 ˚C was analysed by EBSD. A coupled CPFE integrated phase-field model was developed to simulate the SRX kinetics and calculate the recrystallized grain morphology. Additionally, the incubation time for grain nucleation was estimated using the validated model.

### 1.1. Recrystallization process

The term, recrystallization, was defined by Doherty et al. [16] as "the formation of a new grain structure in a deformed material by the formation and migration of high angle boundaries driven by the stored energy of deformation". The recrystallization could be a process of two clear steps, i.e. the formation and then the growth of a stable nucleus in a discontinuous way [3,12]. It is well accepted that the nucleation sites of recrystallization present in the deformed structure can grow further and become new grains once the necessary conditions, such as high angle misorientation and sufficient driving force, are achieved [3,10]. In this regard, the three best-known nucleation theories of recrystallization are the migration of a pre-existing high angle grain boundary (HAGB); the migration of low angle boundaries; and subgrain coalescence [10]. The nucleation by HAGB migration is also known as the theory of strain induced boundary migration (SIBM), verified by Beck and Sperry [12]. In this mechanism, the minimisation of system energy is taken into account by the migration of pre-existing HAGBs toward the interior of a highly strained grain. As shown in Figure 1 a), grain A with low stored energy bugles into grain B with high energy. Hence, the energy reduction associated with the elimination in defects should be larger than the increase of total grain boundary energy due to

bulging in order to initiate this mechanism [10]. For the theory of nucleation by the low angle boundary (i.e. subgrain boundaries) migration suggested by Beck [17] and Cahn [18], subgrains are capable to grow at the expense of its neighbours by the migration of subgrain boundaries. The subgrain boundaries absorb dislocations during growth to increase their misorientation and energy until they transform into high angle grain boundaries (see Figure 1 b). For the theory of nucleation by subgrain coalescence [19], two adjacent subgrains coalescent to form a new grain by lattice rotation (see Figure 1 c). The occurrence of any of these three mechanisms depends on the strain level, heat treatment temperature, stacking fault energy (SFE), subgrain size distribution and the distribution of subgrain misorientation [10].

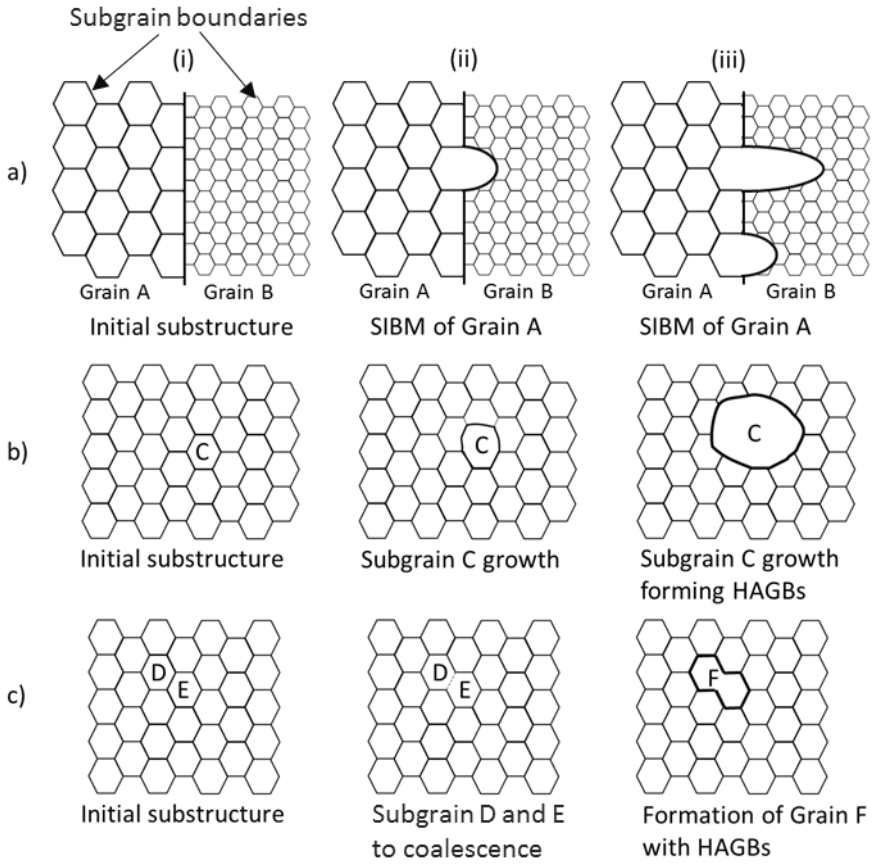



*Figure 1. Schematic representations of three nucleation mechanisms for a recrystallized grain (After Rios [10]). The sequence of (i)-(iii) in a) shows the nucleation by the migration of pre-existing HAGBs; b) shows the nucleation by subgrain boundary migration and HAGBs formation; c) shows the nucleation by coalescence of two subgrains D and E through the "rotation" of one of them.*

As the recrystallization is mostly a site-saturation solid-state reaction, grain growth only occurs after the grain nucleation stage [10]. The driving force of grain growth, in which high

angle grain boundaries (HAGBs) wipe over the strained (non-recrystallized) matrix removing the crystalline defects until the mutual impingement of recrystallized grains, can be continuous (normal grain growth, i.e. primary recrystallization) or discontinuous (abnormal grain growth, i.e. secondary recrystallization) [20]. During normal grain growth, the smallest grains disappear, resulting in a relatively uniform distribution of individual grains size. During abnormal grain growth, however, some of the grains grow rapidly and become much larger than the average [20,21]. Both of these two types of grain coarsening are driven by the reduction in grain boundary area during annealing [10,21].

Under isothermal conditions, primary recrystallization generally shows an incubation time for the formation of nuclei and completion when the recrystallized grains meet mutually [10]. The classic John-Mehl-Avrami-Kolmogorov (JMAK) [22–25] equation has been widely used to predict the overall kinetics of primary recrystallization in deformed metals. The recrystallization fraction $X$ is described by the equation $X = 1 - \exp(-kt^n)$, where $X = 0$ is for the onset of recrystallization and $X = 1$ is for the fully recrystallized material, $t$ is the time, $k$ and $n$ are commonly referred to as the Avrami coefficient and Avrami exponent. In theory, $n$ is equal to 4 if the recrystallization nuclei are randomly distributed, the nucleation rate is constant during annealing, the growth rate is isotropic in three dimensions, and the growth rate of the nuclei remain constant during growth [21]. If the nucleation is site saturated and growth is isotropic in two dimensions [5], then $n$ is equal to 2 and this is exactly the case in this present 2D phase-field simulation work.

### 1.2. KWC phase-field model

The computational model used here to study primary recrystallization is the KWC phase-field model proposed by Kobayashi, Warren and Carter [26]. The energy term in the KWC phase-field model is developed as a function of variables and their gradients, aiming to minimise the total free energy of the system. The microstructure evolution at mesoscale is simulated by two variables, the conserved variable (i.e. phase $\eta$) and the non-conserved variable (i.e. grain orientation $\theta$) [27]. The diffuse-interface approach used in this work, instead of the sharp-interface approach, allows the evolution of arbitrary complex morphologies to be predicted without making any presumptions on the shape of grains [6,9,28]. In the diffuse-interface approach, the grain structure is represented by a set of variables that are continuous in space and time. Within the grain, the phase-field model variables have the same values. At

the grain interface, these variables vary continuously over a narrow range between their equilibrium values in the neighbouring grains [28].

To simulate the grain nucleation at particular sites [3], the KWC phase-field model incorporates separate analytical models into the simulation. In terms of computational effort, it is not feasible to simulate nucleation and grain growth at the same time, as an extremely fine resolution and time step over the whole grain structure are required to catch the occurrence of nucleation [27,28]. Furthermore, it is physically rational to simulate the nucleation and grain growth separately, as the recrystallization is mostly site-saturated [10,29].

The initial deformation state for the phase-field modelling can be obtained based on crystal plasticity finite element (CPFE) simulations [30,31]. According to our previous studies [32–34], the CPFE model used here is able to predict the deformation heterogeneities (e.g. phase interfaces, grain boundaries and their triple points) through coupling the dislocation density (i.e. the sum of GND and SSD) with slip rules [35]. CPFE simulations can help to identify the heterogeneous distribution of nucleation positions and nucleated orientations in the KWC phase-field model [36]. Similarly, the recrystallized microstructure generated by the phase-field model can be imported into the finite element model to predict the mechanical behaviour of the alloy.

## 2. Methodology

### 2.1. Material preparation and quasi-in-situ EBSD characterisation

A rolled sheet of 1050A aluminium was supplied by Aalco Metals Ltd. The chemical composition is listed in Table 1. To study the SRX behaviour of cold rolled single phase aluminium, a rectangular plate 10 (RD)×10 (TD)×6 (ND) $mm^3$ was cut from the rolled sheet, where RD is the rolling direction, TD is the transverse direction and ND is the normal direction for heat treatment.

*Table 1. Chemical composition of 1050A*

| Element | Fe | Si | Zn | Mg | Ti | Mn | Cu | Other | Al |
|---|---|---|---|---|---|---|---|---|---|
| **wt. % up to** | 0.40 | 0.25 | 0.07 | 0.05 | 0.05 | 0.05 | 0.05 | 0.03 | Balance |

The interrupted heat treatment of as received 1050A was carried out in a furnace at 500 ℃ and followed by cold water quenching. The RD-ND surface of cold rolled samples were ground using SiC paper to 1200 grit, then mechanically polished using 40 nm OP-S (Oxide Polishing Suspensions) diluted with $H_2O$ to a ratio 1:5 of OP-S: $H_2O$ for 3 min. Finally, the samples were

electropolished for 60 seconds in a solution of 9.5 vol. % perchloric acid in ethanol at room temperature and 19.5 V, drawing a steady current density of around 0.9 $A/cm^2$.

Electron Backscattered Diffraction (EBSD) was performed in a Carl Zeiss Sigma 300 CrossBeam SEM with Bruker eSprit v2.1 software, using an aperture size of 120 μm and an accelerating voltage of 20 kV with a step size of 3 μm. The EBSD data was analysed using MTEX toolbox [37]. The EBSD scanned area was precisely relocated after further annealing to allow the scanning of the same area. The top, middle and bottom corners of RD-ND plane were quasi-in-situ imaged by EBSD after 0, 5, 10, 52, 105, 527, 1051 and 1667 min annealing at 500 ℃ followed by water quenching. After each heat treatment, the annealed sample was mildly re-polished by 40 nm OPS diluted with $H_2O$ for 2 min and electropolished for 30 seconds. The thickness reduction due to re-polishing was less than 1 μm.

**2.2. Crystal plasticity finite element (CPFE) model**

CPFE models can capture the activation of individual slip systems and the inhibition effect on slip due to the change of grain orientation, thus providing the full-field heterogeneous strain, dislocation density distributions and elastic stress in a grain structure [35]. The model that was used to simulate the deformation state is strain rate sensitive and was implemented in the user material subroutine UMAT using ABAQUS standard analysis [9,32,34,38–41].

The total deformation gradient, **F**, is given by $\mathbf{F} = \mathbf{F^e F^p}$ where $\mathbf{F^e}$ is the elastic deformation gradient and $\mathbf{F^p}$ is the plastic deformation gradient. The lattice rotation and stretch are controlled by the elastic deformation gradient, while the slip and continuum rotation are controlled by the plastic deformation gradient [42].

The rate of deformation, **D**, is expressed as the sum of elastic and plastic rates of deformation as follows

$$\mathbf{D} = \mathbf{D}^{\mathrm{e}} + \mathbf{D}^{\mathrm{p}} \tag{1}$$

where $\mathbf{D^e}$ is determined according to the anisotropic Hook's law and $\mathbf{D^p}$ from the symmetry component of plastic velocity gradient, $\mathbf{L^p}$, as

$$\mathbf{D}^{\mathrm{p}} = \mathrm{sym}(\mathbf{L}^{\mathrm{p}}) \tag{2}$$

where $\mathbf{L^p}$ is given as the sum of contributions to slip from the active slip systems following

$$\mathbf{L}^{\mathrm{p}} = \sum_{\alpha=1}^{12} \dot{\gamma}^{\alpha} \mathbf{s}^{\alpha} \otimes \mathbf{n}^{\alpha} \tag{3}$$

where $\mathbf{s}^{\boldsymbol{\alpha}}$ is the line vector along the slip direction and $\mathbf{n}^{\boldsymbol{\alpha}}$ the slip plane normal of slip system α. The slip rate on the slip system, $\dot{\gamma}^{\alpha}$, is given by dislocation motion overcoming pinning obstacles by means thermal activation as follows

$$\dot{\gamma}^{\alpha} = \rho_{SSD}^{m} v b^2 \exp\left(-\frac{\Delta H}{kT}\right) \sinh\left(-\frac{\Delta V}{kT}\left|\tau^{\alpha} - \tau_c^{\alpha}\right|\right) \tag{4}$$

where $\rho_{SSD}^{m}$ is the density of gliding dislocations, $v$ the jump frequency to overcome obstacle barriers, $b$ the magnitude of the Burger's vector, $\Delta H$ the Helmholtz energy, $k$ the Boltzmann constant, $T$ the temperature in Kelvin, $\Delta V$ the associated activation volume, $\tau_c^{\alpha}$ the critical resolved shear stress of the slip system $\alpha$. Hence, the accumulated slip on the α slip system, $\gamma_{t+\Delta t}^{\alpha}$, after a certain period, $\Delta t$, is expressed as

$$\gamma_{t+\Delta t}^{\alpha} = \gamma_t^{\alpha} + \int_t^{t+\Delta t} \left|\dot{\gamma}^{\alpha}\right| dt = \gamma_t^{\alpha} + \left|\dot{\gamma}_{t+\Delta t}^{\alpha}\right| \Delta t \tag{5}$$

A modified Taylor's dislocation hardening rule to describe the isotropic hardening during plastic deformation is given by

$$\tau_c^{\alpha} = \tau_{c0} + \mu \cdot G_{12} \cdot b \cdot \sqrt{\rho_{GND} + \rho_{SSD}^{S}} \tag{6}$$

where $\tau_{c0}$ is the initial critical resolved shear stress, $\mu$ is the material constant for aluminium [43], $G_{12}$ is the shear modulus, $\rho_{GND}$ is the geometrically necessary dislocation density and $\rho_{SSD}^{S}$ is the density of sessile statistically stored dislocations. $\rho_{SSD}^{S}$ is determined using a phenomenological relation with effective plastic strain, $p$, such that

$$\dot{\rho}_{SSD}^{S} = \lambda \cdot \dot{p} \tag{7}$$

where $\lambda$ is the hardening coefficient and the effective plastic strain rate, $\dot{p}$, is associated with the rate of plastic deformation, $\mathbf{D}^{\mathrm{p}}$, [33] by:

$$\dot{p} = \left(\frac{2}{3}\mathbf{D}^{\mathrm{p}} : \mathbf{D}^{\mathrm{p}}\right)^{1/2} \tag{8}$$

The GNDs are the extra storage of dislocations to accommodate the lattice curvature due to the appearance of non-uniform plastic deformation [44]. The Nye's dislocation tensor to compute the GNDs is given by,

$$\boldsymbol{\Lambda} = \mathrm{curl}\left(\mathbf{F}^{\mathrm{P}}\right) = \sum_{\alpha=1}^{12} \rho_{Gs}^{\alpha} \mathbf{b}^{\alpha} \otimes \mathbf{s}^{\alpha} + \rho_{Get}^{\alpha} \mathbf{b}^{\alpha} \otimes \mathbf{t}^{\alpha} + \rho_{Gen}^{\alpha} \mathbf{b}^{\alpha} \otimes \mathbf{n}^{\alpha} \tag{9}$$

where $\rho_{Gs}^{\alpha}$ are the screw dislocation components on slip system $\alpha$ with line vector along the slip direction $\mathbf{s}^{\alpha}$, $\rho_{Get}^{\alpha}$ and $\rho_{Gen}^{\alpha}$ are the edge dislocation components with line tangent vector along the slip normal $\mathbf{n}^{\alpha}$ and $\mathbf{t}^{\alpha}$, $\mathbf{t}^{\alpha} = \mathbf{s}^{\alpha} \times \mathbf{n}^{\alpha}$ and $\mathbf{b}^{\alpha}$ is the Burgers vector on slip system $\alpha$.

There are 12 $\rho_{Gs}^{\alpha}$ screw, 12 $\rho_{Get}^{\alpha}$ edge and 12 $\rho_{Gen}^{\alpha}$ edge dislocation components, resulting in a total of 36 independent GND components shown in Equation (9). Equation (9) may be written in a matrix form as,

$$\bar{\mathbf{\Lambda}} = \mathbf{A}\rho_{GND} \tag{10}$$

where $\bar{\mathbf{\Lambda}}$ is a 9× 1 vector form of the Nye's dislocation tensor $\mathbf{\Lambda}$, **A** is a 9×36 linear matrix containing the basis tensors $\mathbf{b}^{\alpha}\otimes\mathbf{s}^{\alpha}$, $\mathbf{b}^{\alpha}\otimes\mathbf{t}^{\alpha}$ and $\mathbf{b}^{\alpha}\otimes\mathbf{n}^{\alpha}$. This is an undetermined system of linear equations having infinite solutions. According to the discussion by Arsenlis and Parks [44], the $L_2$ norm is expressed as the sum of the squares of GND densities on each slip system to solve the minimisation problem [45]. The sum of GND densities is given by

$$\rho_{GND} = \sqrt{\sum_{\alpha=1}^{12}\left(\rho_{Gs}^{\alpha}\right)^2 + \left(\rho_{Get}^{\alpha}\right)^2 + \left(\rho_{Gen}^{\alpha}\right)^2} \tag{11}$$

The parameters to simulate the plastic deformation of pure aluminium are listed in Table 2. The initial critical resolved shear stress, $\tau_{c0}$, and the isotropic hardening coefficient, $\lambda$, for $\rho_{SSD}^{S}$ accumulation were calibrated using experimental macroscopic stress-strain response of 1050A (see Figure 2 (b)). The other properties, such as the Young's Modulus, $E$, shear Modulus, $G_{12}$, the magnitude of the Burger's vector, $b$, Boltzmann constant $k$, Helmholtz free energy, $\Delta H$, and activation volume, $\Delta V$, were obtained from the literature for pure aluminium [32,40]. The effects of strain rate sensitivity on the stress response of pure aluminium alloy at room temperature were not considered in the Helmholtz free energy, $\Delta H$, in this study.

A 3D CPFE model (shown in Figure 2 (a)) with the grain morphology and average grain diameter (~120 μm) of the rolled pure aluminium was applied to study the plastic deformation of the alloy 1050A. Twenty-noded brick finite elements with reduced integration (C3D20R) were used in the finite element model. The grain shape was generated by VGRAIN [46] and the grain orientations of 14 grains were determined based on the pole figure of 1050A. Pole figures in Figure 10 a) and b) demonstrate that orientations in CPFE model have a good agreement with the experimental observations. The sample in the simulation was deformed up to 15 % compressive strain under plane strain compression conditions at room temperature to achieve the same amount of GND density of 1050A used in this study. The bottom, left, front and back surfaces are fixed in the model. The dimensions of the polycrystalline sample in the study are 760×760×50 $\mu m^3$.

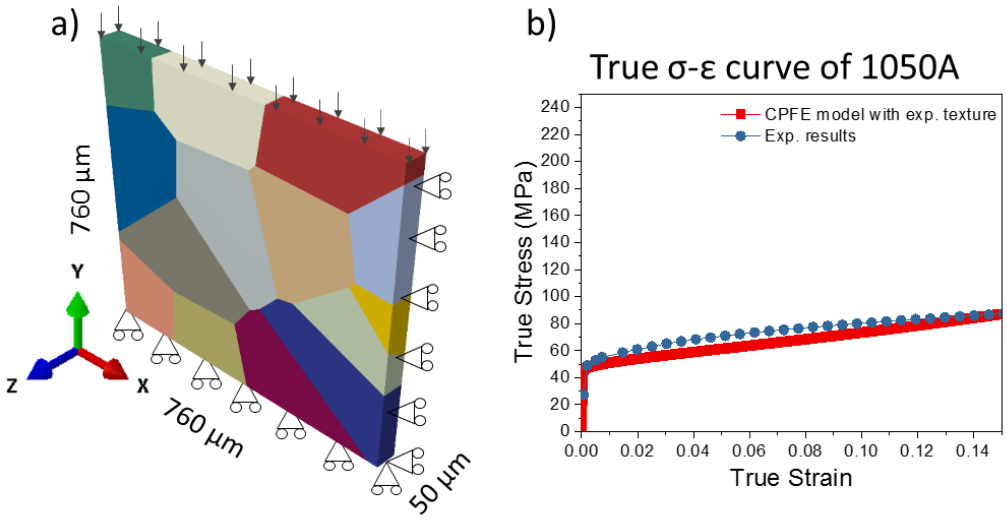



*Figure 2. a) CPFE model of 14 grains with the grain morphology of rolled pure aluminium before the plane strain compression along YY direction. b) The true stress-strain response of the CPFE model and tensile test [68] shows a perfect fit up to 0.15 true strain.*

*Table 2. Material properties of 1050A on CPFE model*

| **Parameter** | k ($JK^{-1}$) | $E$ (MPa) | $G_{12}$ (MPa) | $b$ (µm) | $\tau_c$ (MPa) | $\lambda$ ($\mu m^{-2}$) |
|---|---|---|---|---|---|---|
| **Value** | $1.381\times10^{-23}$ | $70\times10^{3}$ | $26\times10^{3}$ | $2.86\times10^{-4}$ | 21 | 0.1 |
| **Parameter** | $\Delta V$ ($\mu m^2$) | $v$ ($s^{-1}$) | $\rho_{ssd}^{m}$ ($\mu m^{-2}$) | $\Delta H$ (J) | $\mu$ | $T$ (K) |
| **Value** | $6\times10^{-15}\times b^2$ | $1\times10^{11}$ | 0.01 | $2.9\times10^{-20}$ | 0.22 | 293 |

**2.3. Phase-field model**

The crystal orientation and dislocation density (see Figure 3) from CPFE simulation was input for the phase-field model to calculate the grain nucleation and grain growth during recrystallization. Due to the different grid size and irregular element shape, the dislocation density on the mid xy layer was extracted from CPFE model and then remapped using linear interpolation [47,48] before performing the phase-field modelling in 2D. The linear interpolation aims to ensure that the driving force is smoothly distributed within the interface region.

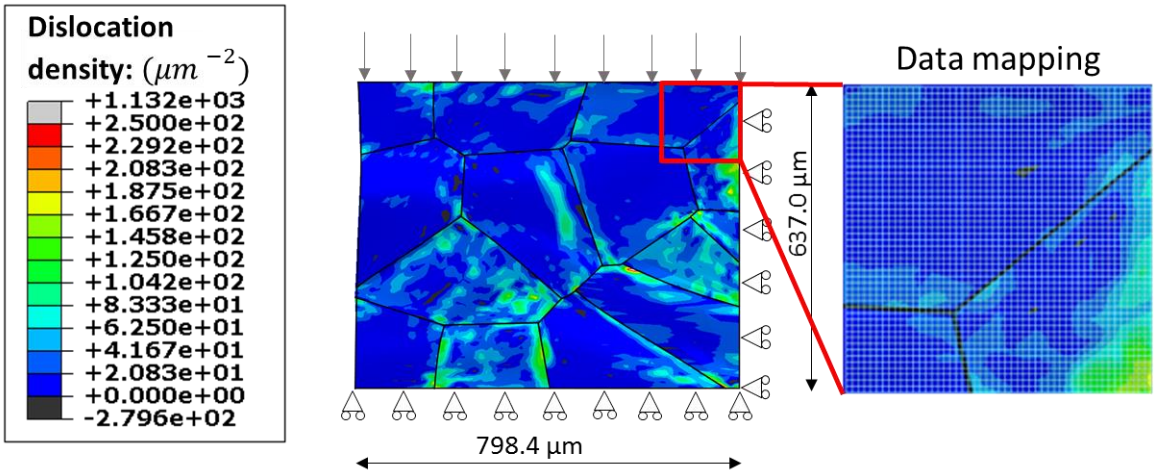



*Figure 3. Dislocation distribution on the xy surface of the deformed CPFE model to 0.15 true strain, where the y-axes are the deformation axes. The simulation results on the elements with irregular shape were remapped to regular shape for the phase-field modelling.*

### 2.3.1. Grain nucleation

To simulate the grain nucleation, the assumption of site-saturated nucleation [29] was applied to the phase-field model. This assumption, verified by Lauridsen et al. [49], states that all nucleation events effectively occur at the start of recrystallization.

The conditions for the grain nucleation [3] are: i) high angle grain boundary; ii) high stored energy; iii) new orientations of nuclei in the deformed structure. Hence, only the grid points at grain boundary with high dislocation density were considered as potential nucleation sites. In this work, the misorientation angle of the grain boundary was set to be more than 15° and $E_c$ was defined to be 0.01 MPa µm$^{-1}$ based on the stored energy distribution shown in Figure 4 a). The orientations of new grains were assigned based on the observations made in the EBSD results (shown in Figure 10). In addition, the minimum distance between two neighbouring nuclei was set to be 50 µm and the grain diameter of seeds was set as 40 µm. The dislocation density ρ and phase distribution $\eta$ after seeding are shown in Figure 4 b) and c).

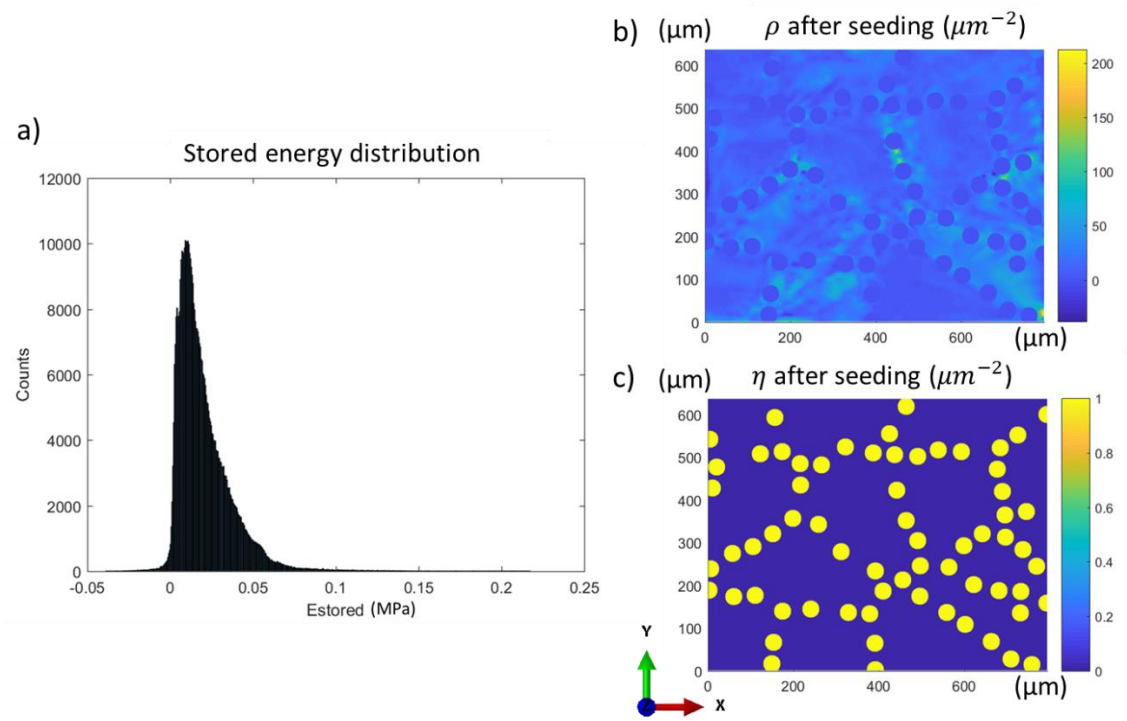



*Figure 4. a) The histogram of stored energy calculated according to Equation (16); b) and c) are the dislocation density ($\rho$) distribution and phase ($\eta$) distribution after seeding. The dislocation density of recrystallized grains was assumed to be 0 $\mu m^{-2}$, and the dislocation density of the deformed grains was extracted from the CPFE model.*

### 2.3.2. Grain growth

The KWC phase-field model [9,50] was selected to model grain growth. Two variables were used to characterise the system. The first variable, $\eta$, was set to be 0 for deformed grains and 1 for recrystallized grains. The second variable, $\theta$, represents the grain orientation. In this model, the orientation in the z-axis was taken to represent the crystal orientation, as the model was performed in two dimensions, i.e. $\theta$ is the value of $\phi_2$ in the Euler angle $[\phi_1, \Phi, \phi_2]$ of the grid point.

The free energy that contains the variables $\eta$ and $\theta$ is expressed by,

$$F = \int \left[ \frac{\alpha^2}{2} |\nabla \eta|^2 + f_d(\eta) + f_e(\eta, \rho) + g(\eta) s |\nabla \theta| \right] dV \tag{12}$$

Hence, the time evolution of $\eta$ and $\theta$ is given by,

$$\dot{\eta} = M_\eta \left\{ \alpha^2 \nabla^2 \eta - \frac{\partial f_d(\eta)}{\partial \eta} - \frac{\partial f_e(\eta, \rho)}{\partial \eta} - \frac{\partial g(\eta)}{\partial \eta} s |\nabla \theta| \right\} \tag{13}$$

$$\dot{\theta} = M_\theta \frac{1}{\eta^2} \nabla \left[ g(\eta) s \frac{\nabla \theta}{|\nabla \theta|} \right] \tag{14}$$

The homogeneous bulk free energy term [28], $f_e(\eta,\rho)$, in Equation (13) is expressed as,

$$f_e(\eta,\rho) = f_e^r(\rho)\,p(\eta) + f_e^m(\rho)\big(1-p(\eta)\big) \tag{15}$$

where $f_e(\eta,\rho)$ is an interpolation function that combines the free energy expressions of the deformed phase $f_e^m(\rho)$ and recrystallized phase $f_e^r(\rho)$. The bulk energies of each phase were calculated based on the dislocation density. Also, the dislocation density in the recrystallized grain is found to be around five orders smaller than that of the deformed grain [30]. Therefore, the free energy in the recrystallized phase $f_e^r(\rho) = 0$ and in the deformed phase $f_e^m(\rho) = 50E_{store}$ have been chosen, where the stored energy per unit length (i.e. per micrometre) of a deformed alloy $E_{store}$ is given by Reed-Hill et al. [51],

$$E_{store} = 0.5\rho G_{12} b^2 \tag{16}$$

where $\rho$ is the dislocation density, $G_{12}$ is the shear modulus of aluminium alloy and $b$ is the Burger's vector magnitude.

$p(\eta)$ in Equation (15) is a weight function used to smooth the density inside the interface region and is defined as follows,

$$p(\eta) = \eta^3\left(10 - 15\eta + 6\eta^2\right) \tag{17}$$

Both of $q(\eta)$ and $p(\eta)$ are used to construct the homogeneous free energy density $f_e(\eta,\rho)$ for the deformed and recrystallized phase [28]. The interfacial energy term [28], $f_d(\eta)$, in equation (13) is expressed as,

$$f_d(\eta) = Wq(\eta) \tag{18}$$

$$q(\eta) = \eta^2(1-\eta)^2 \tag{19}$$

$$W = \frac{6\sigma a}{\delta} \tag{20}$$

where $q(\eta)$ is a double-well potential that has minima at 0 and 1, and $W$ is the depth of the energy wall. The double-well coefficient, $W$, is a constant and can be modified by adjusting the grain boundary thickness, $\delta$, and grain boundary energy, $\sigma$.

The gradient energy term, $\frac{\alpha^2}{2}|\nabla\eta|^2$, gives rise to the diffuse interface. The gradient coefficient, $\alpha$, expressed in Equation (21) is a constant associated with $\delta$ and $\sigma$.

$$\alpha = \sqrt{\frac{3\delta\sigma}{a}} \tag{21}$$

where $a = 2.20$ for an interface region with $\eta \in [0.1,0.9]$. The grain boundary thickness is given based on the theory of diffuse interface approach [28] by,

$$\delta = 4\Delta x \tag{22}$$

where $\Delta x$ is the grid size.

The orientation energy term, $g(\eta)s|\nabla\theta|$, penalising grain misorientation is given by,

$$g(\eta)=\eta^2 \tag{23}$$

$$s=\frac{6\sigma}{\pi} \tag{24}$$

where the function $g(\eta)$ is used to eliminate the effect of misorientation inside the deformed grain. The constant $s$ is related to the interface energy, $\sigma$.

The mobilities of $\eta$ and $\theta$ are expressed as $M_\eta$ and $M_\theta$. The expression of $M_\eta$ when $\Delta\theta = 0$, which considers steady grain growth in a one dimension problem [30], is given by

$$M_\eta = M_0 \exp(-\frac{Q}{RT}) = M_0 \exp(-\frac{Q'}{k_B T}) \tag{25}$$

where $M_0$ is a pre-exponential factor, $Q$ and $Q'$ are the activation energies, $R$ is the gas constant, $T$ is the annealing temperature and $k_B$ is the Boltzmann constant.

The mobilities used to define the rate of change in grain orientation are defined as follows:

$$M_\theta=\left(1-p(\eta)\right)M_\theta^0 \tag{26}$$

$$M_\theta^0=M_\eta \tag{27}$$

The grain growth of nucleated grains driven by the stored energy follows the time-evolution of $\eta$ and $\theta$ as described by Equation (13) and (14). The evolution of the 2D microstructure is solved using finite difference, with an eighth-order scheme for the spatial derivatives and the Euler Forward method for time integration.

The parameters used in the phase-field model to simulate the SRX of deformed pure aluminium at 773 $K$ (i.e. 500 ℃) are listed in Table 3.

*Table 3. Material properties of deformed 1050A on the KWC phase-field model*

| **Parameter** | $\Delta x$ (μm) | $\sigma$ (J/m$^2$) | $T$ (K) | $k_B$ (J/K) | $a$ | $Q'$ (J) | $\Delta t$ (ms) | $M_0$ (m$^3$/(N ms)) |
|---|---|---|---|---|---|---|---|---|
| **value** | 2 | 0.6 | 773 | $1.381\times10^{-23}$ | 2.20 | $2.08\times10^{-19}$ | 0.01 | $3.1\times10^{7}$ |

# 3. Results

## 3.1. EBSD results

The quasi-in-situ EBSD maps at the top, middle and bottom corners of the cold rolled pure Al RD-ND plane were applied to characterise the grain size, recrystallization fraction, texture, GND distribution and fraction of high angle grain boundaries (HAGBs) during annealing. The HAGBs are the grain boundaries with misorientation of $> 15°$ [2].

### 3.1.1. Texture evolution

The quasi-in-situ inverse pole figure (IPF) EBSD maps taken for the rolling direction (RD) are shown in Figure 5 a). The maps of each row were captured from the same area. The corresponding pole figures (PF) at each corner but from a bigger area are plotted in Figure 5 c).

The evolution of the PF shows the change of texture at each corner during annealing. As shown in Figure 5 c), the texture varied slightly between the area near the edge of the rolled sample and the area in the middle, due to the different deformation states of the rolled sheet during rolling. However, the texture at each corner remained the same during the annealing no matter how long the recrystallization occurred. This notable observation is an important support for the texture simulation in the phase-field model. The nucleated grains tend to keep the orientation of deformed grains in the pure aluminium, thus maintaining the texture.

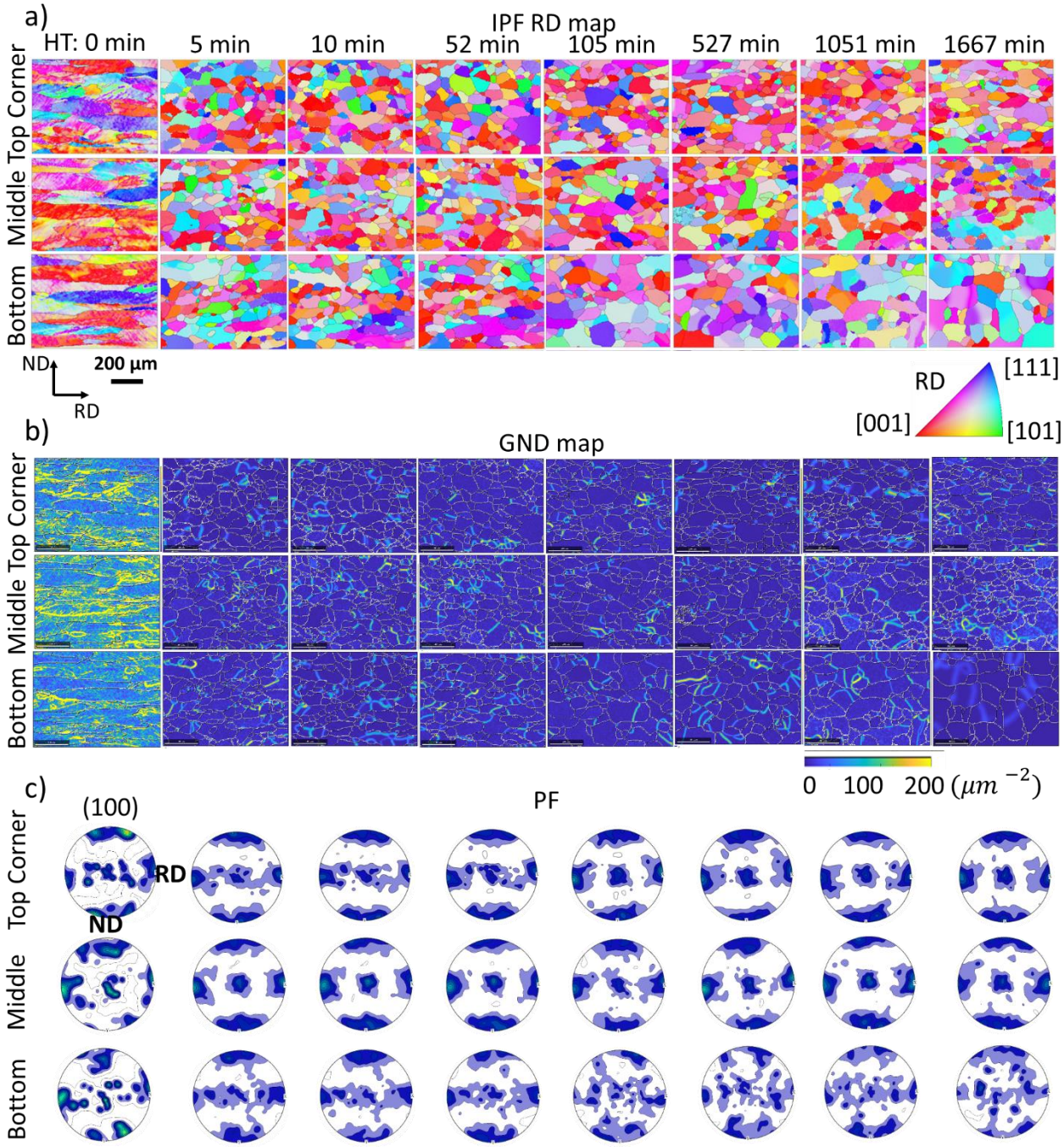



*Figure 5. EBSD a) IPF maps b) GND density maps and c) PF of cold rolled pure aluminium 1050A at the top, middle and bottom corners after 0, 5, 10, 52, 105, 527, 1051 and 1667 min annealing at 500 ℃. The rolling direction (RD) is horizontal, and observation along RD was applied to IPF triangle. The (001) pole figures are shown in the same orientation as the IPF maps.*

**3.1.2. Grain size and HAGBs fraction evolution**

To calculate the average grain size of the recrystallized grains, the grains that have grain orientation spread (GOS) values lower than 2° are recognised as recrystallized grains [52,53]. In Figure 6 a), the plots show the average grain size and recrystallized grain size evolution at each corner. The average grain diameter reduced rapidly from over 100 µm to around 60 µm after 5 min of annealing and remained at ~60 µm with further annealing. The recrystallized grain diameter grew quickly from 0 µm to around 60 µm after 5 min of annealing and remained at ~60 µm.

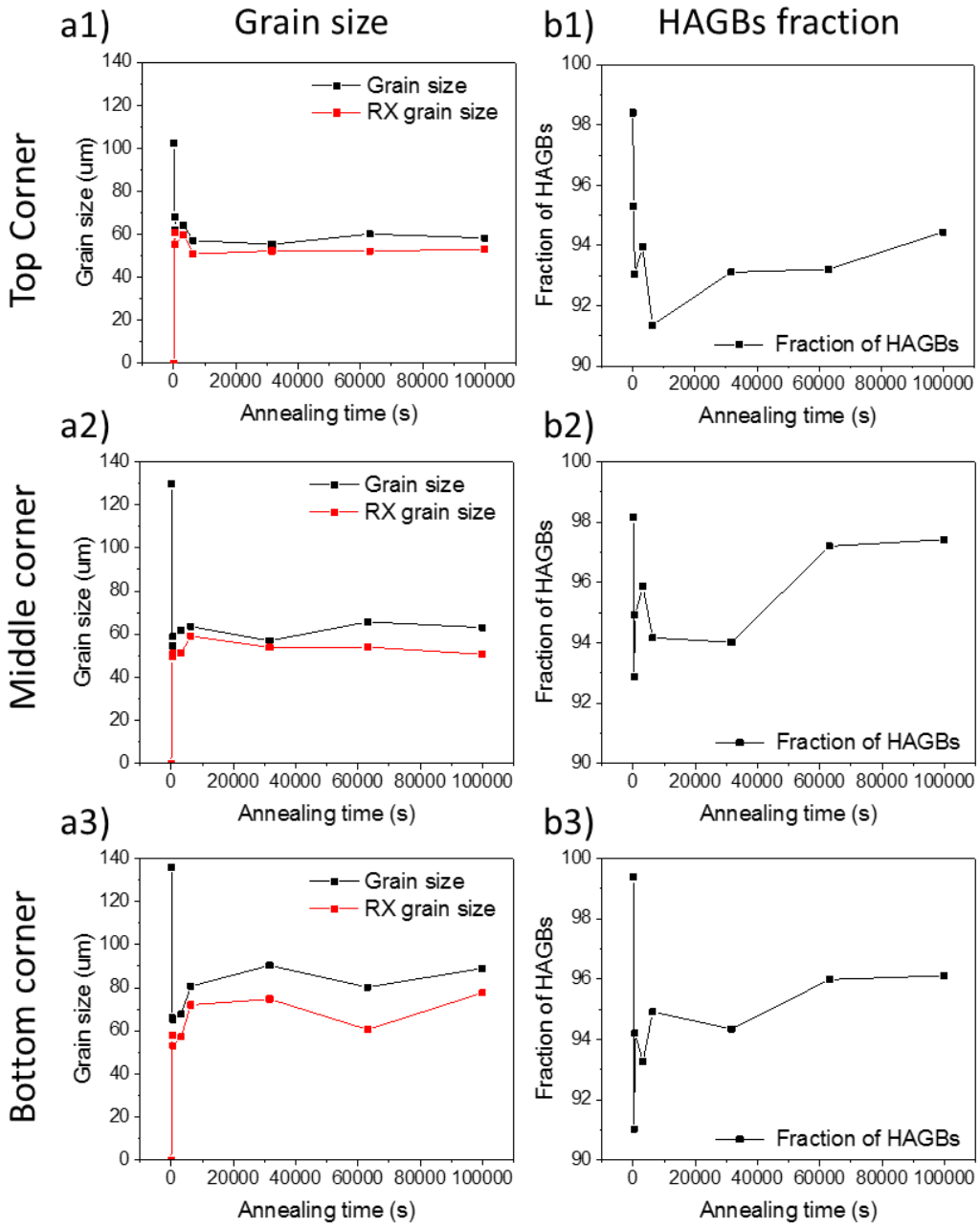



*Figure 6. a) Average grain diameter and recrystallized grain diameter evolution on top, middle and bottom corners after 0, 5, 10, 52, 105, 527, 1051 and 1667 min annealing at*

*500 ℃. b) The evolution of high angle grain boundaries (HAGBs) fraction during annealing.*

The quasi-in-situ EBSD maps were zoomed in to investigate how the microstructure changed during annealing to determine the nucleation mechanism in pure aluminium. An example is shown in Figure 7. Subgrains were found within the recrystallized grain, such as the Grain A in Figure 7 b), with an orientation variation inside it. The subgrain boundaries transformed into the HAGBs and formed separate grains during further annealing (see Figure 7 c)). Thus, the evolution of the average grain size fluctuated with the annealing time due to the separation of growing grains. The plots of HAGBs fraction in Figure 6 b) show that the fraction of HAGBs increases with annealing. These results validate the nucleation theory as seen in Figure 1 a) and b), and explain why the average grain size does not grow during annealing.

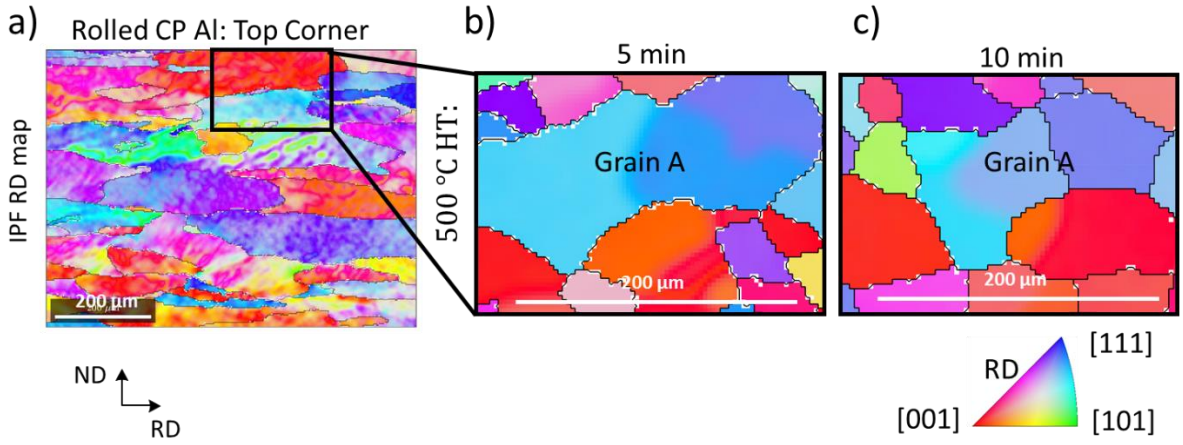



*Figure 7. EBSD IPF maps of a small area on the top corner of cold rolled pure aluminium 1050A after a)-c) 0, 5 and 10 min annealing at 500℃. b) and c) show how the subgrain boundaries in recrystallized grain A were accumulated during annealing to form separated grains.*

### 3.1.3. Hardness evolution

The hardness evolution shown in Figure 8 was obtained by performing the Vickers hardness tests using a load of 5 kg on the sample annealed for different times at 500 ℃. The hardness of the pure aluminium depends on dislocations and grain size only, due to the absence of any alloying precipitates. The hardness of cold rolled pure aluminium dropped rapidly from HV5 38 to 20 after 5 min of annealing due to the elimination of dislocations by recrystallization. The hardness of the annealed samples remained constant at around HV5 20 during annealing, while the hardening is mainly caused by grain boundaries after full recrystallization as described by the Hall-Petch relation [54]. This macroscopic mechanical behaviour of annealed

pure aluminium also demonstrates that grain size does not vary greatly in the annealed sample since the effects of grain boundary hardening are similar for the sample at the different annealing times.

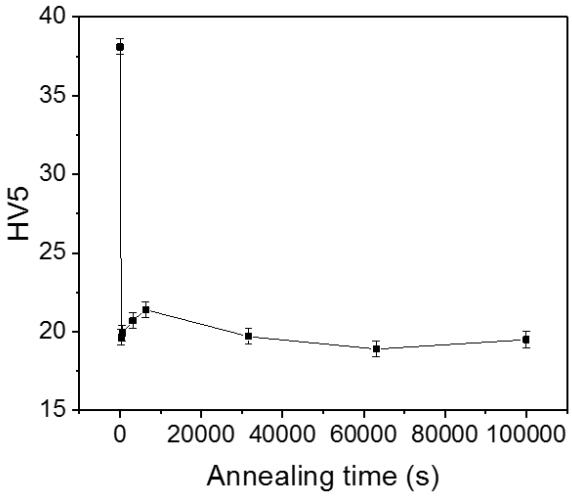



*Figure 8. Macroscopic hardness results on the cold rolled pure Al that annealed for 0, 5, 10, 52, 105, 527, 1051 and 1667 min at 500℃.*

**3.1.4. The evolution of GND density and recrystallization fraction**

The geometrically necessary dislocation (GND) distribution was calculated using the method in [55] and plotted in Figure 5 b). The displacement gradient tensor was obtained first from the orientation map. The lattice rotation corresponding to the antisymmetric part of the displacement tensor was thus resolved. The lower bound of the GND density was then estimated from the lattice rotation gradients [55,56]. Subgrain boundaries observed in the GND maps are the positions with high values of GND inside of the grain.

The evolution of the recrystallization fraction during annealing, shown in Figure 9 a), was quantitatively analysed based on the kernel average misorientation (KAM) as calculated from the EBSD maps. The KAM is an average misorientation of a point with respect to all its neighbours, i.e. a measure of local deviation in orientation. The areas with KAM values less than the threshold value ($0.5°$ in this work), were recognised as new deformation-free, recrystallized areas [57].

As shown in Figure 9 a) and b), the recrystallization completed in 5 min, resulting in a quick reduction of GND from $\sim 100\ \mu m^{-2}$ to $\sim 10\ \mu m^{-2}$ in 5 min. The slight fluctuation of recrystallization fraction and GND density during further annealing was due to the area change of grain boundaries. The evolution of recrystallization fraction at the top corner was plotted in

Figure 13 a) together with the JMAK theoretical curve and the curve from the phase-field model.

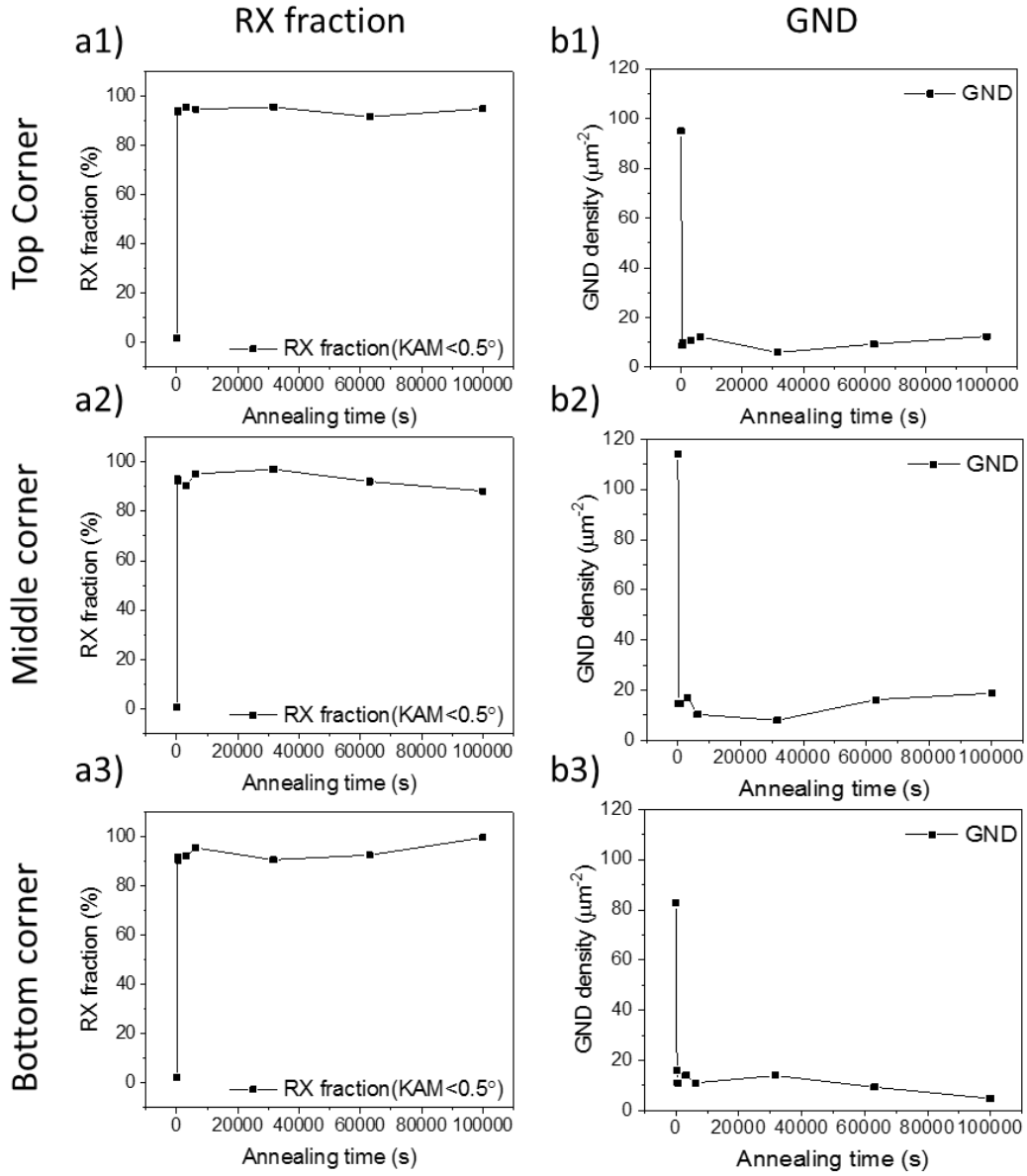



*Figure 9. a) Recrystallization fraction values calculated based on the KAM maps on top, middle and bottom corners after 0, 5, 10, 52, 105, 527, 1051 and 1667 min annealing at 500 ℃. b) The evolution of geometrically necessary dislocation density (GND) during annealing.*

### 3.2. CPFE results

The xy face of the CPFE model, with the boundary conditions of plane strain compression, was plotted in Figure 3. The colour represents the dislocation density distribution, which is the

sum of GND and SSD densities. The nucleation positions of the new grains during annealing were determined based on this dislocation distribution (shown in Figure 4).

### 3.3. Phase-field model results

#### 3.3.1. Simulated texture evolution

The orientations of the nucleated grains were assigned based on the rolled sample. According to the experimental observation on the texture evolution shown in Section 3.1.1, the recrystallized texture remained close to that of the deformed texture in the mesoscale. Hence, the simulated deformation and recrystallized texture in this work were assigned to have the same texture as in the experiments. The consistency of the texture in modelling and experiment was verified by comparing their IPF maps and PF (see Figure 10).

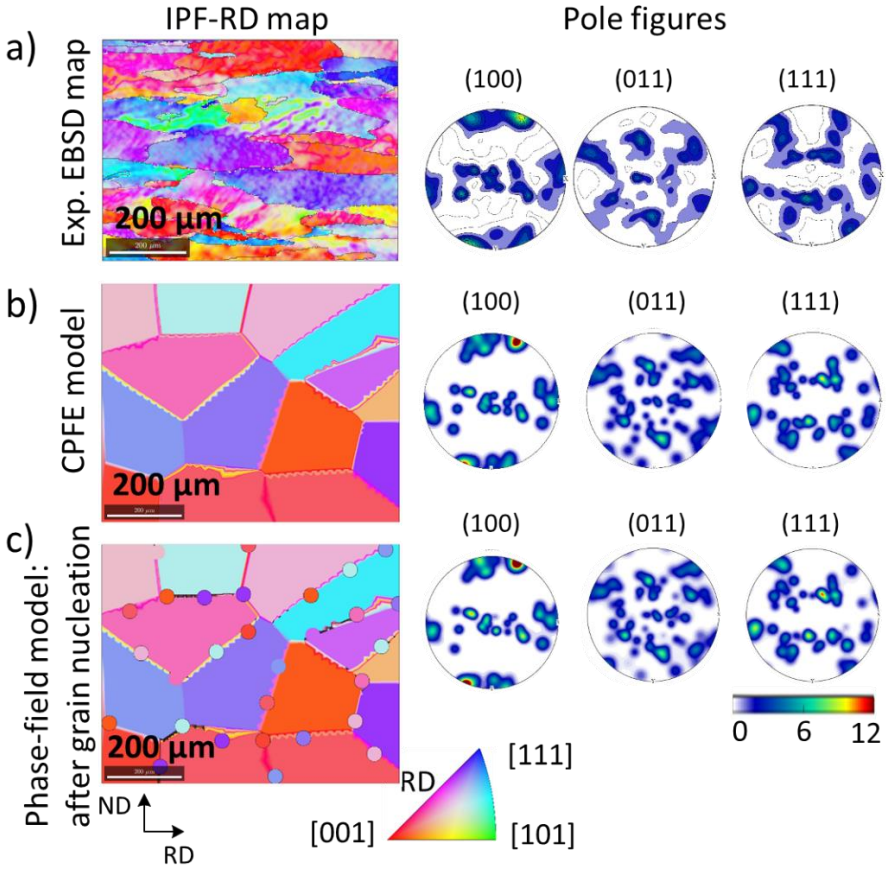



*Figure 10. a)-c) are the IPF-RD maps and PF of the grain orientations in EBSD map, in deformed CPFE model and in the phase-field model after the simulation of grain nucleation.*

#### 3.3.2. Simulated recrystallization fraction evolution

Figure 11 shows the simulated evolution during annealing at 500 ℃ of a) the recrystallized phase and b) grain orientations. The recrystallized phase with low energy during annealing is

shown to bulge into the neighbouring deformed phase with high stored energy and thus reduce total stored energy. The grain growth described by Equation (13) and (14) was quantitatively analysed by measuring the grain size and RX fraction at each time step and plotted in Figure 13 together with the JMAK and experimental results. As the grain nucleation in this work occurred at the beginning of the RX, the time for nucleated grains to reach the critical diameter of 40 μm at 500 ℃ was estimated to be 40 s according to the initial area fraction of the recrystallized phase, which is 0.157, in the phase-field model. The critical grain diameter was set to be 40 μm according to the size of small grains shown in the recrystallized EBSD maps (see column a) and c) in Figure 12).

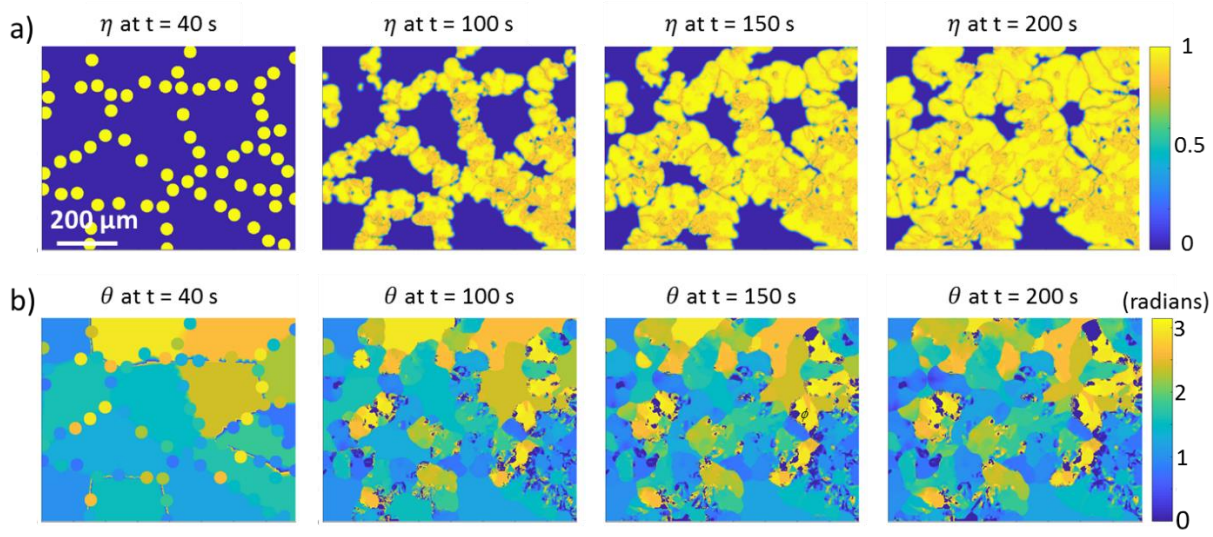



*Figure 11. a) and b) show the change of two order parameters* $\eta$ *and* $\theta$ *after 40* $s$ *, 100* $s$ *, 150* $s$ *and 200* $s$ *annealing at 500℃ obtained by the KWC phase-field model.*

### 3.3.3. Simulated grain size evolution

The orientation evolution simulated by the KWC phase-field model was processed using the grain construction in MTEX toolbox [37] to obtain the grain structure (see Figure 12). Column a) and b) in Figure 12 show the grain structure from the top corner EBSD maps and phase-field simulations after 0, 5, 10, 52 and 105 min of annealing at 500 ℃. The grain area distributions for experimental results and simulated results are shown in column c) and d) correspondingly.

A comparison between column c) and d) in Figure 12 reveals that the phase-field model predicts the grain area distribution accurately after the completion of recrystallization, i.e. after 5 min. The simulated grains after full RX generally had an area size of less than $1.5\times 10^4$ $\mu m^2$, with only a few of them having an area larger than this. Furthermore, in terms of the average

grain size, the simulated evolution agreed well with the experimental results as shown in Figure 13 b), especially when the annealing time is longer than 10 min.

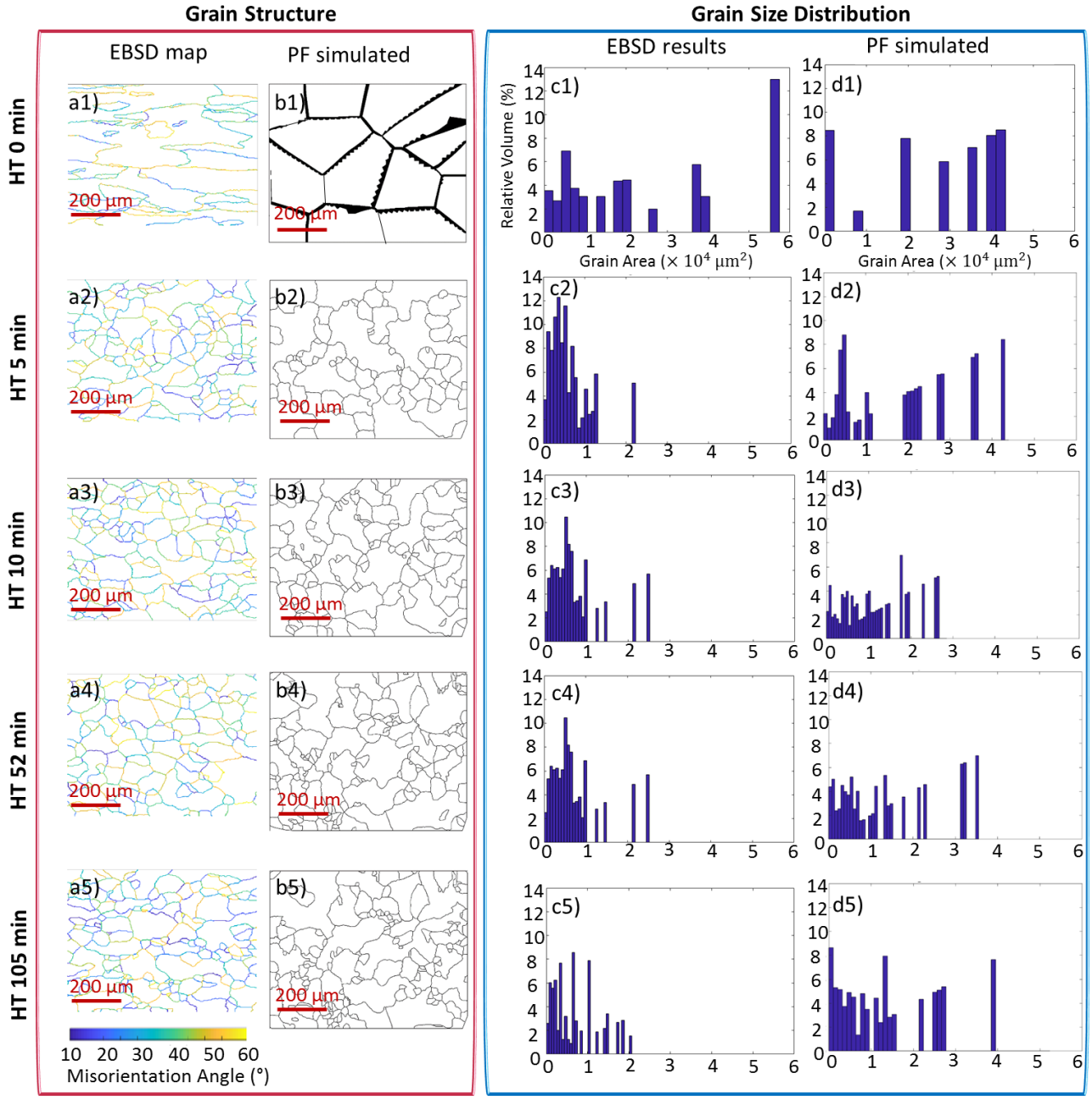



*Figure 12. Column a)-b) and c)-d) are the grain structures and histograms of grain area from EBSD mapping and phase-field modelling respectively, after 0, 5, 10, 52 and 10 min annealing at 500℃. The grain boundaries shown in a1)-a5) are coloured to show their misorientation angle.*

### 3.4. JMAK curve

Based on the previous discussion, the Avrami exponent $n = 2$ was selected for the JMAK curve of rolled pure aluminium alloy, which was heated at 500 ℃. The Avrami coefficient

k=5.625× $10^{-5}$ was chosen by calibrating the JMAK equation with the experimental EBSD results. As the maximum RX fraction is 0.95 due to the existence of high angle grain boundaries (see Figure 12), the JMAK curve has been modified to the equation below and plotted in Figure 13 a):

$$X = 0.95 \times [1 - \exp(-5.625 \times 10^{-5} \times t^2)] \quad (28)$$

# 4. Discussion

## 4.1. Experimental observations

Through tracking the microstructure evolution during SRX using quasi-in-situ EBSD maps, the mechanisms of grain nucleation and grain growth in the rolled pure aluminium were revealed. Furthermore, the validation of the phase-field model was achieved by the evolution of microstructural features characterised by EBSD.

In terms of the grain nucleation, subgrain boundaries absorbed dislocations during annealing, resulting in an increase of misorientation, stored energy and mobility, thus, leading to the transformation into HAGBs and the formation of grains [2]. This explains why the fraction of HAGBs increased with annealing and why the recrystallized grains grew to $\sim 60\ \mu m$ diameter in the first 5 min and then kept constant during annealing (see Figure 6). The simultaneous processes of grain splitting and grain growth accounted for the dynamic stability of grain size during annealing. In terms of grain coarsening, pre-existing HAGBs migrated toward the interior of a more highly strained grain to minimise the total energy of the system, as described by the SIBM theory [10,58].

In addition, the grain nucleated by subgrain boundary migration maintained the orientation of the subgrain while its orientation was originally generated from the deformed structure. Thus, it is straightforward to account for the consistency between the recrystallized texture and the deformed texture in Figure 5 c). Therefore, the nucleation mechanism of pure aluminium can be described by the migration of pre-existing subgrains or grain boundaries [10].

## 4.2. Modelling results

### 4.2.1. Prediction of texture and nucleation positions

The heterogeneous distribution of dislocation density and the accumulation of dislocations at grain boundaries in the textured model under plane strain compression were captured by the CPFE model in this work. This dislocation distribution and grain orientation information were then used as initial conditions for the phase-field model, making the prediction of nucleated grain orientations and nucleation positions in the deformed structure possible. The model

described in this paper can be adapted to study other materials by incorporating the effects of precipitates, material properties etc.

### 4.2.2. Prediction of incubation time

The phase-field model coupled with theoretical JMAK kinetics provides insights into the nucleation mechanism regarding the estimation of incubation time and its relation to dislocation density and annealing temperature, which are hard to be captured by experiments. In this work, the incubation time was determined as ~ 40 s to reach the recrystallization fraction of 15.7 % with the critical recrystallized grain diameter of 40 µm (see Figure 13 a)).

### 4.2.3. Prediction of recrystallization fraction evolution

The simulated evolution curve agrees well with the EBSD results and JMAK curve in Figure 13 a), indicating that the phenomena of the grain nucleation and the impingement of growing grains for moderate grain growth were successfully simulated. The KWC phase-field modelling in this work considers the energy from dislocations, the interface energy and the misorientation energy.

### 4.2.4. Prediction on the distribution and evolution of grain size

The phase-field model together with the CPFE model was able to provide a reliable prediction of the grain size distribution and evolution for pure aluminium after full RX (see Figure 12 b) and Figure 13 b)). The slight variation of grain size distribution between experiments and simulation in initial observation (see Figure 12 c2) and d2)) is likely due to the choice of nucleation condition for critical stored energy. The in-situ EBSD mapping for the SRX of rolled pure aluminium could help to determine this value by observing the minimum grain size and calculating the GND density at the nucleation position before and after the nucleation. As a result, the grain size at partial RX could then be accurately predicted.

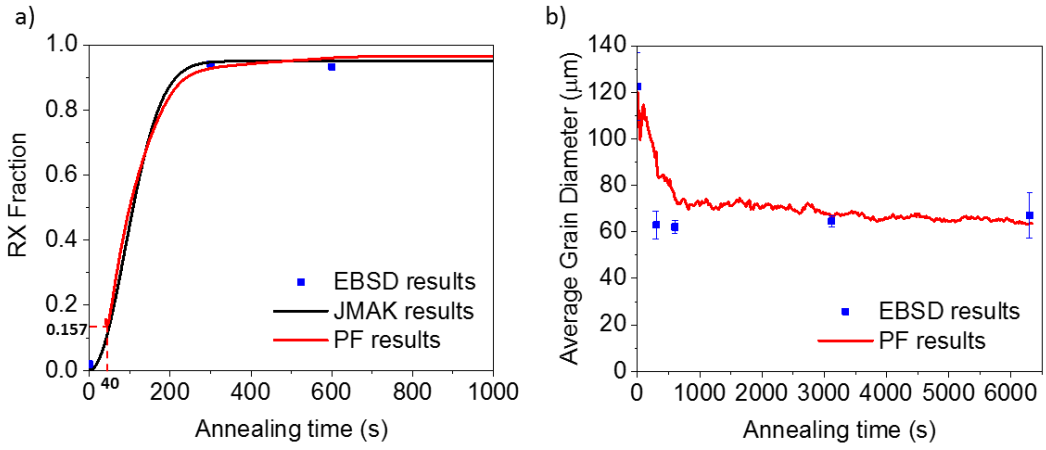


*Figure 13. The evolutions of a) recrystallization fraction and b) average grain diameter at 500 ℃ heat treatment from experimental EBSD results, phase-field (PF) modelling and theoretical JMAK curve.*

### 4.3. Importance

Compared to traditional models, the phase-field model coupled with CPFE analysis is able to predict the nucleated grains and grain growth according to the thermodynamic law by obtaining the heterogeneous deformed microstructure from CPFE. Through changing the boundary conditions, for example, the strain paths in the CPFE model and the temperature gradients in the phase-field model, the prediction of RX under complex strain paths and temperature gradients become feasible for the industry. Furthermore, it is challenging to determine the incubation time and verify the relationship between incubation time, GND density and annealing time from experiments. Our phase-field modelling work together with theoretical JMAK equation presented here offers a solution to this problem. Additionally, with regard to the prediction of texture evolution, the KWC phase-field model has the capability of generating orientations for new grains from experimental observations, theoretical hypothesis and physical principles. The conditions for the grain nucleation in this work could be modified for different materials by the inclusion of further parameters, such as solutes, precipitates and crystal structure. Conversely, the recrystallized microstructure can be input into a crystal plasticity model as the initial conditions in future work to achieve the prediction of the mechanical properties, such as the strength [59], ductility [60], creep [61], fatigue [62] and stress crack corrosion behaviour [63] of load-bearing components.

## 5. Conclusions

The SRX features of rolled pure aluminium, with regard to grain size evolution, RX fraction evolution and texture evolution were characterised by the quasi-in-situ EBSD. Based on observation of the stable grain size and the consistency of texture during recrystallization, the nucleation mechanism of AA1050 could be attributed to the migration of subgrain boundaries and SIBM. This leads to a) splitting of the grain during grain coarsening due to the transformation of subgrain boundaries into HAGBs; and b) maintenance of the deformed texture during annealing.

In terms of the grain nucleation, the developed KWC phase-field model identified the favourable orientations and positions for nucleation on the basis of the heterogeneous deformed microstructure from the CPFE model. The incubation time for grain nucleation was estimated

by using a comparison between the simulated results, experimental evolution and theoretical JMAK curve.

In terms of grain growth, the KWC phase-field model perfectly simulated the grain coarsening and the impingement of recrystallized grains by calculating the energy reduction of the system during annealing. Furthermore, the grain boundary curvature solved by this model would be particularly useful in the prediction of the mechanical properties according to the grain size distribution and the grain shape.

In conclusion, the proposed KWC phase-field model and the CPFE model including physical length and time scales, provide versatile tools for simulating the microstructural evolution during recrystallization. The quasi-in-situ EBSD results achieved in the experimental work are in a good agreement with the simulated texture development, grain size distribution and its evolution. The validated model also provides insight on the incubation time and nucleation conditions. The results presented here indicate that the phase-field and CPFE models form a good basis for the prediction of material behaviour following thermomechanical treatment.

## Author Contributions

QL devised this work and conducted mechanical testing, EBSD characterisation, CPFE model, phase-field model calibration and data analysation. JL conducted the phase-field model construction. JJ and JZ supervised the work. All authors contributed to drafting the final manuscript.

## Acknowledgements

The strong support from the Aviation Industry Corporation of China (AVIC), the First Aircraft Institute (FAI), China Scholarship Council (CSC), the Henry Lester Trust and the Great Britain-China Educational Trust for this funded research is much appreciated. The research was performed at the AVIC Centre for Structural Design and Manufacture at Imperial College London. EBSD Microscopy was carried out within the Harvey Flower Electron Microscopy Suite at Imperial College. We would like to thank Drs Mahmoud Ardakani for training and support of instrument usage, gratefully thank Zebang Zheng for his assistance on CPFE modelling, Vassili A Vorontsov and Christopher Gourlay for helpful discussions on the phase-field modelling. The authors would also like to thank the funding support by EPSRC under the Grant Agreement EP/R001715/1 on “LightForm: Embedding Materials Engineering in Manufacturing with Light Alloys”.

## References

[1] K.G.F. Janssens, D. Raabe, E. Kozeschnik, M.A. Miodownik, B. Nestler, Computational materials engineering : an introduction to microstructure evolution, Elsevier / Academic Press, 2007.
[2] K. Huang, K. Marthinsen, Q. Zhao, R.E. Logé, The double-edge effect of second-phase particles on the recrystallization behaviour and associated mechanical properties of metallic materials, Prog. Mater. Sci. 92 (2018) 284–359. doi:10.1016/j.pmatsci.2017.10.004.
[3] F.J. Humphreys, M. Hatherly, Recrystallization and related annealing phenomena, Elsevier, 2004. doi:10.1016/B978-008044164-1/50014-1.
[4] D. Raabe, 23 - Recovery and Recrystallization: Phenomena, Physics, Models, Simulation, in: Elsevier, Oxford, 2014: pp. 2291–2397. doi:10.1016/B978-0-444-53770-6.00023-X.
[5] A.D. Rollett, Overview of modeling and simulation of recrystallization, Prog. Mater. Sci. 42 (1997) 79–99. doi:10.1016/S0079-6425(97)00008-X.
[6] H. Hallberg, Approaches to modeling of recrystallization, Metals (Basel). 1 (2011) 16–48. doi:10.3390/met1010016.
[7] P. Bate, Modelling deformation microstructure with the crystal plasticity finite-element method, Philos. Trans. R. Soc. A Math. Phys. Eng. Sci. 357 (1999) 1589–1601. doi:10.1098/rsta.1999.0391.
[8] D. Raabe, R.C. Becker, Coupling of a crystal plasticity finite-element model with a probabilistic cellular automaton for simulating primary recrystallization in aluminium, Model. Simul. Mater. Sci. Eng. 8 (2000) 445–462. doi:10.1002/3527606157.ch1.
[9] Q. Luan, J. Lee, Z. Zheng, J. Lin, J. Jiang, Static recrystallization study on pure aluminium using crystal plasticity finite element and phase-field modelling, Procedia Manuf. 15 (2018) 1800–1807. doi:10.1016/J.PROMFG.2018.07.211.
[10] P.R. Rios, F. Siciliano, H. Ricardo, Z. Sandim, R.L. Plaut, A. Fernando Padilha, Nucleation and growth during recrystallization, Mater. Res. 8 (2005) 225–238. doi:10.1590/S1516-14392005000300002.
[11] I.L. Dillamore, C.J.E. Smith, T.W. Watson, Oriented nucleation in the formation of annealing textures in iron, Met. Sci. J. 1 (1967) 49–54. doi:10.1179/msc.1967.1.1.49.
[12] P.A. Beck, P.R. Sperry, C.S. Smith, J.E. Burke, P.R. Sperry, C.S. Smith, J.E. Burke, Strain induced grain boundary migration in high purity aluminum, J. Appl. Phys. 21 (1950) 150–152. doi:10.1063/1.1699614.
[13] D. Raabe, Multiscale recrystallization models for the prediction of crystallographic textures with respect to process simulation, J. Strain Anal. Eng. Des. 42 (2007) 253–268. doi:10.1243/03093247JSA219.
[14] H.S. Ubhi, J. Parsons, N. Othen, S. Campbell, R. Poole, a Gholinia, In-situ EBSD Phase Transformation and Recrystallisation, J. Phys. Conf. Ser. 522 (2014) 12011. doi:10.1088/1742-6596/522/1/012011.
[15] J. Lin, Fundamentals of Materials Modelling for Metals Processing Technologies, Imperial College Press, 2015. doi:10.1142/p951.
[16] R.D. Doherty, R.W. Cahn, Nucleation of new grains in recrystallization of cold-worked metals, J. Less Common Met. 28 (1972) 279–296. doi:10.1016/0022-5088(72)90131-2.
[17] P.A. Beck, The Formation of Recrystallization Nuclei, J. Appl. Phys. 20 (1949) 633–634. doi:10.1063/1.1698446.
[18] R.W. Cahn, A New Theory of Recrystallization Nuclei, Proc. Phys. Soc. Sect. A. 63 (1950) 323–336. doi:10.1088/0370-1298/63/4/302.
[19] W. Boas, J.S. Bowles, The effect of crystal arrangement on " secondary recrystallization" in metals, J. Inst. Met. 74 (1947) 501–519.

[20] M. Hillert, On the theory of normal and abnormal grain growth, Acta Metall. 13 (1965) 227–238. doi:10.1016/0001-6160(65)90200-2.
[21] R.D. Doherty, D.A. Hughes, F.J. Humphreys, J.J. Jonas, D.J. Jensen, M.E. Kassner, W.E. King, T.R. McNelley, H.J. McQueen, A.D. Rollett, Current issues in recrystallization: a review, Mater. Sci. Eng. A. 238 (1997) 219–274. doi:10.1016/S0921-5093(97)00424-3.
[22] A.N. Shiryayev, On The Statistical Theory of Metal Crystallization, in: Sel. Work. A. N. Kolmogorov, Springer Netherlands, Dordrecht, 1992: pp. 188–192. doi:10.1007/978-94-011-2260-3_22.
[23] W.A. Johnson, R.F. Mehl, Reaction kinetics in processes of nucleation and growth, Trans. Am. Inst. Min. Met. Eng. 135 (1939) 416–442.
[24] M. Avrami, Kinetics of Phase Change. I General Theory, J. Chem. Phys. 7 (1939) 1103. doi:10.1063/1.1750380.
[25] M. Avrami, Kinetics of Phase Change. II Transformation-Time Relations for Random Distribution of Nuclei, J. Chem. Phys. 8 (1940) 212. doi:10.1063/1.1750631.
[26] R. Kobayashi, J.A. Warren, W.C. Carter, A continuum model of grain boundaries, Phys. D Nonlinear Phenom. 140 (2000) 141–150. doi:https://doi.org/10.1016/S0167-2789(00)00023-3.
[27] M. Muramatsu, Y. Aoyagi, Y. Tadano, K. Shizawa, Phase-field simulation of static recrystallization considering nucleation from subgrains and nucleus growth with incubation period, Comput. Mater. Sci. 87 (2014) 112–122. doi:10.1016/j.commatsci.2014.02.003.
[28] N. Moelans, B. Blanpain, P. Wollants, An introduction to phase-field modeling of microstructure evolution, Calphad Comput. Coupling Phase Diagrams Thermochem. 32 (2008) 268–294. doi:10.1016/j.calphad.2007.11.003.
[29] K. Marthinsen, E. Nes, O. Daaland, T. Furu, The spatial distribution of nucleation sites and its effect on recrystallization kinetics in commercial aluminum alloys, Metall. Mater. Trans. A. 34 (2003) 2705–2715. doi:10.1007/s11661-003-0172-3.
[30] T. Takaki, A. Yamanaka, Y. Higa, Y. Tomita, Phase-field model during static recrystallization based on crystal-plasticity theory, J. Comput. Mater. Des. 14 (2007) 75–84. doi:10.1007/s10820-007-9083-8.
[31] L. Gránásy, T. Pusztai, J.A. Warren, S. Biswas, I. Samajdar, A. Haldar, A. Sain, Coarsening in polycrystalline material using quaternions, J. Phys. Condens. Matter. 23 (2011) 72202–5. doi:10.1088/0953-8984/23/7/072202.
[32] Y. Guan, B. Chen, J. Zou, T. Ben Britton, J. Jiang, F.P.E.E. Dunne, Crystal plasticity modelling and HR-DIC measurement of slip activation and strain localization in single and oligo-crystal Ni alloys under fatigue, Int. J. Plast. 88 (2017) 70–88. doi:10.1016/j.ijplas.2016.10.001.
[33] B. Chen, J. Jiang, F.P.E. Dunne, Is stored energy density the primary meso-scale mechanistic driver for fatigue crack nucleation?, Int. J. Plast. 101 (2018) 213–229. doi:10.1016/J.IJPLAS.2017.11.005.
[34] B. Chen, J. Jiang, F.P.E. Dunne, Microstructurally-sensitive fatigue crack nucleation in Ni-based single and oligo crystals, J. Mech. Phys. Solids. 106 (2017) 15–33. https://www.sciencedirect.com/science/article/pii/S0022509617301059 (accessed June 7, 2017).
[35] F.P.E. Dunne, R. Kiwanuka, A.J. Wilkinson, Crystal plasticity analysis of micro-deformation, lattice rotation and geometrically necessary dislocation density, Proc. R. Soc. A Math. Phys. Eng. Sci. 468 (2012) 2509–2531. doi:10.1098/rspa.2012.0050.
[36] K. Adam, D. Zöllner, D.P. Field, 3D microstructural evolution of primary recrystallization and grain growth in cold rolled single-phase aluminum alloys, Model.

Simul. Mater. Sci. Eng. 26 (2018). doi:10.1088/1361-651X/aaa146.
[37] F. Bachmann, R. Hielscher, H. Schaeben, Texture Analysis with MTEX – Free and Open Source Software Toolbox, Solid State Phenom. 160 (2010) 63–68. doi:10.4028/www.scientific.net/SSP.160.63.
[38] F.P.E. Dunne, D. Rugg, A. Walker, Lengthscale-dependent, elastically anisotropic, physically-based hcp crystal plasticity: Application to cold-dwell fatigue in Ti alloys, Int. J. Plast. 23 (2007) 1061–1083. doi:10.1016/j.ijplas.2006.10.013.
[39] V.V.C. Wan, M.A. Cuddihy, J. Jiang, D.W. MacLachlan, F.P.E. Dunne, An HR-EBSD and computational crystal plasticity investigation of microstructural stress distributions and fatigue hotspots in polycrystalline copper, Acta Mater. 115 (2016) 45–57. doi:10.1016/j.actamat.2016.05.033.
[40] T. Zhang, D.M. Collins, F.P.E.E. Dunne, B.A. Shollock, Crystal plasticity and high-resolution electron backscatter diffraction analysis of full-field polycrystal Ni superalloy strains and rotations under thermal loading, Acta Mater. 80 (2014) 25–38. doi:10.1016/j.actamat.2014.07.036.
[41] T. Zhang, J. Jiang, B. Britton, B. Shollock, F. Dunne, Crack nucleation using combined crystal plasticity modelling, high-resolution digital image correlation and high-resolution electron backscatter diffraction in a superalloy containing non-metallic inclusions under fatigue, Proc. R. Soc. London A Math. Phys. Eng. Sci. 472 (2016). http://rspa.royalsocietypublishing.org/content/472/2189/20150792 (accessed June 19, 2017).
[42] F.P.E. Dunne, Introduction to computational plasticity, Oxford University Press, Oxford ; New York, 2005.
[43] M.E. Kassner, A case for Taylor hardening during primary and steady-state creep in alurniniurn and type 304 stainless steel, J. Mater. Sci. 25 (1990). https://link.springer.com/content/pdf/10.1007%2FBF01045755.pdf (accessed August 21, 2017).
[44] A. Arsenlis, D.. Parks, Crystallographic aspects of geometrically-necessary and statistically-stored dislocation density, Acta Mater. 47 (1999) 1597–1611. doi:10.1016/S1359-6454(99)00020-8.
[45] J. Cheng, S. Ghosh, A crystal plasticity FE model for deformation with twin nucleation in magnesium alloys, Int. J. Plast. 67 (2015) 148–170. https://www.sciencedirect.com/science/article/pii/S0749641914001995 (accessed June 9, 2017).
[46] P. Zhang, D. Balint, J. Lin, An integrated scheme for crystal plasticity analysis: Virtual grain structure generation, Comput. Mater. Sci. 50 (2011) 2854–2864. doi:10.1016/j.commatsci.2011.04.041.
[47] M.J. Powell, T. Physics, S. Street, A direct search optimization method that models the objective and constraint functions by linear interpolation, in: Adv. Optim. Numer. Anal., Springer, 1994: pp. 51–67.
[48] P. Zhao, T. Song En Low, Y. Wang, S.R. Niezgoda, An integrated full-field model of concurrent plastic deformation and microstructure evolution: Application to 3D simulation of dynamic recrystallization in polycrystalline copper, Int. J. Plast. 80 (2016) 38–55. doi:10.1016/J.IJPLAS.2015.12.010.
[49] E.M. Lauridsen, H.F. Poulsen, S.F. Nielsen, D. Juul Jensen, Recrystallization kinetics of individual bulk grains in 90% cold-rolled aluminium, Acta Mater. 51 (2003) 4423–4435. doi:10.1016/S1359-6454(03)00278-7.
[50] J.A. Warren, R. Kobayashi, A.E. Lobkovsky, W.C. Carter, Extending phase field models of solidification to polycrystalline materials, Acta Mater. 51 (2003) 6035–6058.

[51] R.E. Reed-Hill, R. Abbaschian, R. Abbaschian, Physical metallurgy principles, Van Nostrand New York, 1973.
[52] K. Radwański, Application of FEG-SEM and EBSD Methods for the Analysis of the Restoration Processes Occurring during Continuous Annealing of Dual-Phase Steel Strips, Steel Res. Int. 86 (2015) 1379–1390. doi:10.1002/srin.201400361.
[53] N. Peranio, Y.J. Li, F. Roters, D. Raabe, Microstructure and texture evolution in dual-phase steels: Competition between recovery, recrystallization, and phase transformation, Mater. Sci. Eng. A. 527 (2010) 4161–4168. doi:10.1016/j.msea.2010.03.028.
[54] N. Hansen, Hall–Petch relation and boundary strengthening, Scr. Mater. 51 (2004) 801–806. doi:10.1016/J.SCRIPTAMAT.2004.06.002.
[55] W. Pantleon, Resolving the geometrically necessary dislocation content by conventional electron backscattering diffraction, Scr. Mater. 58 (2008) 994–997. doi:10.1016/J.SCRIPTAMAT.2008.01.050.
[56] J.W. Kysar, Y. Saito, M.S. Oztop, D. Lee, W.T. Huh, Experimental lower bounds on geometrically necessary dislocation density, Int. J. Plast. 26 (2010) 1097–1123. doi:10.1016/J.IJPLAS.2010.03.009.
[57] Z. Liu, R.O. Olivares, Y. Lei, C.I. Garcia, G. Wang, Microstructural characterization and recrystallization kinetics modeling of annealing cold-rolled vanadium microalloyed HSLA steels, J. Alloys Compd. 679 (2016) 293–301. doi:10.1016/j.jallcom.2016.04.057.
[58] K. Huang, R.E. Logé, A review of dynamic recrystallization phenomena in metallic materials, Mater. Des. 111 (2016) 548–574. doi:10.1016/J.MATDES.2016.09.012.
[59] Y.S. Sato, H. Kokawa, Distribution of tensile property and microstructure in friction stir weld of 6063 aluminum, Metall. Mater. Trans. A. 32 (2001) 3023–3031. doi:10.1007/s11661-001-0177-8.
[60] D. Witkin, Z. Lee, R. Rodriguez, S. Nutt, E. Lavernia, Al–Mg alloy engineered with bimodal grain size for high strength and increased ductility, Scr. Mater. 49 (2003) 297–302. doi:10.1016/S1359-6462(03)00283-5.
[61] A.K. Ghosh, R. Raj, Grain size distribution effects in superplasticity, Acta Metall. 29 (1981) 607–616. doi:10.1016/0001-6160(81)90142-5.
[62] A.M. Korsunsky, D. Dini, F.P.E. Dunne, M.J. Walsh, Comparative assessment of dissipated energy and other fatigue criteria, Int. J. Fatigue. 29 (2007) 1990–1995. doi:10.1016/J.IJFATIGUE.2007.01.007.
[63] V.Y. Gertsman, S.M. Bruemmer, Study of grain boundary character along intergranular stress corrosion crack paths in austenitic alloys, Acta Mater. 49 (2001) 1589–1598. doi:10.1016/S1359-6454(01)00064-7.
[64] I. Brough, J. Humphreys, D. McDonald, A. Gholinia, P. Bate, An investigation of dynamic recrystallisation on Cu–Sn bronze using 3D EBSD, Mater. Sci. Technol. 26 (2010) 685–690. doi:10.1179/026708309x12547309760966.
[65] D. Juul Jensen, R.B.N. Godiksen, Neutron and Synchrotron X-ray Studies of Recrystallization Kinetics, Metall. Mater. Trans. A. 39 (2008) 3065–3069. doi:10.1007/s11661-008-9613-3.
[66] G. Ischia, H.-R. Wenk, L. Lutterotti, F. Berberich, Quantitative Rietveld texture analysis of zirconium from single synchrotron diffraction images, J. Appl. Crystallogr. 38 (2005) 377–380. doi:10.1107/S0021889805006059.
[67] J. Gastaldi, C. Jourdan, New possibilities for recrystallization study by X-Ray synchrotron radiation topography, Phys. Status Solidi. 49 (1978) 529–537. doi:10.1002/pssa.2210490213.
[68] F. Djavanroodi, M. Daneshtalab, M. Ebrahimi, A novel technique to increase strain distribution homogeneity for ECAPed materials, Mater. Sci. Eng. A. 535 (2012) 115–

121. doi:10.1016/j.msea.2011.12.050.